Check for updates

CoWO$_4$ nanoparticles with dual active sites for highly efficient ammonia synthesis†

Lian Duan,‡[a] Zhencong Huang,‡[a] Gen Chen,[a] Min Liu, [iD][b] Xiaohe Liu,[c] Renzhi Ma [iD] *[d] and Ning Zhang [iD] *[a]

The electrochemical reduction reaction of NO$_3^-$ (NO$_3$RR) represents a promising green technology for ammonia (NH$_3$) synthesis. Among various electrocatalysts, Co-based materials have demonstrated considerable potential for the NO$_3$RR. However, the NH$_3$ production efficiency of Co-based materials is still limited due to challenges in the competitive hydrogen evolution reaction (HER) and hydrogenating oxynitride intermediates (*NO$_x$). In this study, tungsten (W) and cobalt (Co) elements are co-incorporated to form cobalt tungstate (CoWO$_4$) nanoparticles with

[a] *School of Materials Science and Engineering, Central South University, Changsha, 410083, China. E-mail: nzhang@csu.edu.cn*

[b] *School of Physics and Electronics, Central South University, Changsha, 410083, China*

[c] *School of Chemical Engineering, Zhengzhou University, Zhengzhou, 450001, China*

[d] *Research Center for Materials Nanoarchitectonics (MANA), National Institute for Materials Science (NIMS), Tsukuba, Ibaraki, 305-0044, Japan. E-mail: ma.renzhi@nims.go.jp*

† Electronic supplementary information (ESI) available: Experimental section, supplementary figures and tables. See DOI: https://doi.org/10.1039/d5nh00120j

‡ These authors contributed equally to this work.

New concepts

Tungsten and cobalt elements are co-incorporated to form cobalt tungstate (CoWO$_4$) nanoparticles, which feature bimetallic W and Co active sites. These nanoparticles are employed to optimize the hydrogenation of *NO$_x$ and suppress hydrogen evolution reactions, thereby facilitating highly efficient NO$_3^-$ reduction to NH$_3$. Theoretical calculations reveal that Co sites in CoWO$_4$ promote the adsorption and hydrogenation of *NO$_x$ intermediates, while W sites inhibit the competing hydrogen evolution reaction (HER). These dual active sites work synergistically to enhance NH$_3$ production during NO$_3^-$ reduction. Guided by these computational insights, CoWO$_4$ nanoparticles are synthesized *via* a simple ion precipitation method, with sizes ranging from 10 to 30 nm. Electrochemical testing demonstrates that CoWO$_4$ nanoparticles achieve a high faradaic efficiency of 97.8 $\pm$ 1.5% and an NH$_3$ yield of 13.2 mg h^{-1} cm^{-2}, significantly outperforming the corresponding WO$_3$ and Co$_3$O$_4$ materials as well as most reported electrocatalysts. *In situ* Fourier transform infrared spectroscopy reveals the enhanced adsorption and hydrogenation of *NO$_x$ intermediates and the suppression of the HER on CoWO$_4$, which contributes to the high efficiency and selectivity toward NH$_3$. This study presents a simple yet effective strategy for the design and synthesis of electrocatalytic materials by precisely tailoring active sites with distinct functions, which advances the development of highly efficient electrocatalysts for NH$_3$ production.

dual active sites of Co^{2+} and W^{6+}, which are applied to optimize the hydrogenation of NO$_x$ and decrease the HER, thereby achieving a highly efficient NO$_3$RR to NH$_3$. Theoretical calculations indicate that the Co sites in CoWO$_4$ facilitate the adsorption and hydrogenation of *NO$_x$ intermediates, while W sites suppress the competitive HER. These dual active sites work synergistically to enhance NH$_3$ production from the NO$_3$RR. Inspired by these calculations, CoWO$_4$ nanoparticles are synthesized using a simple ion precipitation method, with sizes ranging from 10 to 30 nm. Electrochemical performance tests demonstrate that CoWO$_4$ nanoparticles exhibit a high faradaic efficiency of 97.8 $\pm$ 1.5% and an NH$_3$ yield of 13.2 mg h^{-1} cm^{-2}. *In situ* Fourier transform infrared spectroscopy characterizes the enhanced adsorption and hydrogenation behaviors of *NO$_x$ as well as a minimized HER on CoWO$_4$, which contributes to the high efficiency and selectivity to NH$_3$. This work introduces CoWO$_4$ nanoparticles as an electrocatalytic material with dual active sites, contributing to the design of electrocatalysts for NH$_3$ synthesis.

1. Introduction

Ammonia (NH_3) is essential for producing fertilizers and nitrogen compounds, largely *via* the Haber–Bosch process, which synthesizes NH_3 from N_2 and H_2.[1] Due to the high energy required to break the $N{\equiv}N$ bond (941 kJ mol^{-1}), this process requires extreme temperatures (400–600 °C) and pressures (200–300 atm).[2,3] The required H_2 comes from methane steam reforming, generating substantial CO_2 emissions, contributing to environmental concerns.[4,5] Electrocatalytic synthesis offers an eco-friendly, energy-efficient method for NH_3 production using renewable resources.[6–8] While the nitrogen reduction reaction (NRR) is promising, challenges such as the hydrogen evolution reaction (HER), low N_2 solubility, and the high dissociation energy of the $N{\equiv}N$ bond limit faradaic efficiency and NH_3 yield.[9,10] Using nitrate (NO_3^-) instead of N_2 improves water solubility and reduces the energy required for bond dissociation, making it an ideal nitrogen source.[11–13] Moreover, the NO_3^- reduction reaction (NO_3RR) can convert wastewater pollutants into NH_3, offering a strategy to balance the nitrogen cycle.[14–16] However, the NO_3RR is a complex, slow process requiring eight-electron transfer, and it generates by-products like NO_2^-, N_2, and H_2.[17,18] Effective hydrogenation of adsorbed oxynitride intermediates ($*NO_x$, *e.g.*, $*NO_3$ and $*NO_2$) and suppressed HER during the catalytic process are important to enhance the formation of NH_3.[19,20]

Transition metal-based oxide electrocatalytic materials, such as NiO, Co_3O_4, Fe_2O_3, and MnO_2, have been demonstrated to exhibit high hydrolysis dissociation activity and distinct electrocatalytic activity for the HER or oxygen evolution reaction (OER).[21–24] In the context of the NO_3RR, their remarkable hydrolysis dissociation capability provides substantial quantities of $*H$ for the hydrogenation of NO_x intermediates. Among them, Co based materials are promising electrocatalysts due to the strong electrostatic interaction of Co 3d electrons with NO_3^- as well as strong hydrolysis dissociation capability to provide $*H$ for hydrogenation of NO_x intermediates.[25,26] For example, Zhang *et al.* reported electron-deficient Co metal nanocrystals for improving both NO_3^- adsorption and $*NH$ hydrogenation to enhance the NH_3 production in the NO_3RR.[27] Gu *et al.* designed ultrathin CoO_x nanosheets with abundant adsorbed oxygen species, which hampers the HER on cobalt oxide and leads to an enhanced NO_3RR activity.[28] Lu *et al.* synthesized a Co_3O_4 nanosheet array with cobalt vacancies on carbon cloth, which exhibited a high faradaic efficiency.[29] However, competitive HER generally occurs intensively on most Co based materials within aqueous electroreduction systems, which hinders the selectivity of the NO_3RR and causes a decrease of NH_3 production efficiency.

On the other hand, tungsten (W) based oxide materials such as WO_3 are regarded as a prospective electrocatalyst for the NO_3RR due to its low cost, strong electronegativity, and excellent electrochemical stability.[30,31] Prior research indicates that the 5d electron orbital of W exhibited an exceptionally robust adsorption capacity for reactive hydrogen, impeding the desorption of $*H$ and contributing to the suboptimal HER.[32] From the perspective of electrocatalytic NO_3RR, a stronger $*H$ adsorption capacity and low tendency for the HER are favourable for achieving efficient NH_3 production.[33,34] However, for pristine WO_3 materials, the too sluggish HER resulting from strong $*H$ adsorption introduces a high energy barrier for hydrogenation of $*NO_x$, thereby restricting its involvement in the hydrogenation process and causing the excessive formation of NO_2^-. Therefore, it is essential to maintain a balanced state for NO_x hydrogenation and the HER.

In this work, tungsten oxides and cobalt oxides are co-incorporated to form cobalt tungstate ($CoWO_4$) with bimetallic Co–W dual active sites to optimize the hydrogenation of $*NO_x$ intermediates and decrease the HER process to enhance the electrochemical NO_3RR to NH_3. Density functional theory (DFT) calculations predict that Co sites in $CoWO_4$ benefit the adsorption and hydrogenation of NO_x intermediates, while W sites decrease water dissociation and the HER, which exhibits a synergistic high efficiency in electrocatalytic reduction of NO_3^- to NH_3. Inspired by DFT calculations, the $CoWO_4$ nanoparticles are synthesized via a one-step precipitation method. $CoWO_4$ exhibits excellent NO_3RR performance across a broad potential range, spanning from −0.2 to −0.7 V *versus* the reversible hydrogen electrode (*vs.* RHE). At a potential of −0.4 V, the maximum Faraday efficiency (FE) of NH_3 generation on $CoWO_4$ is 97.8 ± 1.5%, which is significantly higher than that of WO_3 (60.1 ± 5.8%) and Co_3O_4 (83.9 ± 5.1%). *In situ* Fourier-transform infrared (FT-IR) spectroscopy further confirms that $CoWO_4$ not only enhances the hydrogenation of $*NO_x$ intermediates but also minimizes the HER, thus facilitating efficient NO_3RR to produce NH_3. This work offers an effective strategy to engineer high performance NO_3RR electrocatalysts based on bimetallic oxides.

2. Experimental

2.1 Synthesis of $CoWO_4$ nanoparticles

$CoWO_4$ nanoparticles were synthesized by an ion precipitation method. In a typical procedure, 1.455 g of $Co(NO_3)_2 \cdot 6H_2O$ (5 mmol) and 1.649 g of $Na_2WO_4 \cdot 2H_2O$ (5 mmol) were added into 60 mL deionized water. Then, the solution was mixed and heated to 70 °C for 3 hours with constant stirring. The resulting suspension and precipitate were subjected to washing with deionized water and ethanol, followed by several rounds of centrifugation. Finally, the $CoWO_4$ powder was obtained through oven drying.

2.2 Synthesis of WO_3 and Co_3O_4 nanoparticles

In the preparation of Co_3O_4 nanoparticles, 20 mL of 0.5 M Na_2CO_3 was added dropwise to the solution of $Co(NO_3)_2 \cdot 6H_2O$ (0.291 g dissolved in 20 mL deionized water) under constant stirring. In order to synthesize WO_3 nanoparticles, 20 mL of 0.1 M HCl was added dropwise to a solution of sodium tungstate (0.329 g dissolved in 20 mL deionized water) under constant stirring. Subsequently, the mixed solution was subjected to a series of washes with deionized water and ethanol, followed by several rounds of centrifugation. The precipitate obtained following drying was subjected to calcination in a muffle furnace at 500 °C in air for a period of two hours,

resulting in the formation of Co_3O_4 and WO_3 nanoparticles, respectively.

Details on the electrocatalytic performance tests, DFT computations, characterizations, NH_3 and NO_2^- quantification, faradaic efficiency and yield rate calculations, and *in situ* measurements are described in the ESI.†

3. Results and discussion

3.1 Theoretical calculations

DFT calculations were initially employed to investigate the adsorption properties of $*NO_x$ intermediates and $*H_2O$ species over the surface of WO_3, Co_3O_4, and $CoWO_4$. The (001) surfaces of WO_3, Co_3O_4, and $CoWO_4$ were constructed for calculations (Fig. 1a), and additional DFT computational details could be found in the ESI.† As illustrated in Fig. 1b, the adsorption energies of $*NO_3$ and $*NO_2$ on WO_3, Co_3O_4, and $CoWO_4$ surfaces were initially investigated. From the calculated values in Fig. 1c, it can be observed that the adsorption energies of $*NO_3$ on the surfaces of the catalysts are 0.55, −0.75, and −0.86 eV for WO_3, $CoWO_4$, and Co_3O_4, respectively. And we also investigated the adsorption energies of $*NO_3$ on the Co and W sites of $CoWO_4$ and electron transfer between active sites and NO_3^- (Fig. S1, ESI†). The adsorption of $*NO_3$ is more favourable at the Co sites than at the W sites, suggesting that the NO_3RR is more likely to occur at the Co sites. And the adsorption energies of $*NO_2$ on the surfaces of catalysts are −0.45, −1.63, and −2.07 eV for WO_3, $CoWO_4$, and Co_3O_4, respectively. The $*NO_2$ is thus more easily adsorbed on Co_3O_4 and $CoWO_4$.

Subsequently, the Gibbs free energy for each reaction step on these catalyst surfaces was calculated to examine the effect of $*NO_x$ adsorption on the reaction pathway of the NO_3RR (atomic models are shown in Fig. S2–S4, ESI†). We considered that the reaction pathways from NO_3^- to NH_3 are as follows: $(*+NO_3^-) \rightarrow *NO_3 \rightarrow *NO_3H \rightarrow *NO_2 \rightarrow *NO_2H \rightarrow *NO \rightarrow *NOH \rightarrow *N \rightarrow *NH \rightarrow *NH_2 \rightarrow *NH_3$.[35] As presented in Fig. 1d, the results of the calculated Gibbs free energies demonstrate that the formation of $*NO_3$ intermediates on the $CoWO_4$ and Co_3O_4 surfaces exhibits a negative free energy, indicating that $CoWO_4$ and Co_3O_4 have a strong adsorption capacity for NO_3^-. Furthermore, the maximum reaction Gibbs free energy change (ΔG_{max}) of the NO_3RR on WO_3, $CoWO_4$, and Co_3O_4 occurs in the step of $*NO_2$ to $*NO_2H$, suggesting that the hydrogenation of $*NO_2$ is the rate-determining step (RDS) of the reaction. Fig. 1e illustrates the ΔG_{max} of the hydrogenation of $*NO_2$ to $*NO_2H$ on WO_3, Co_3O_4 and $CoWO_4$, which are 1.64, 1.42 and 1.04 eV, respectively. It is evident that the $CoWO_4$ lowers the reaction energy barrier of the RDS, which is favourable to the $*NO_2$ hydrogenation process.

The H_2O dissociation process on WO_3, Co_3O_4, and $CoWO_4$ is also investigated (Fig. S5–S8, ESI†). Fig. S5 (ESI†) shows that the stronger adsorption of $*H$ and H_2O occurs more easily on the W sites than on the Co sites in $CoWO_4$, indicating that hydrolysis process occurs predominantly on the W sites. The calculation results of the H_2O dissociation process in Fig. 1f demonstrate that the hydrolysis barrier on $CoWO_4$ is lower than

that on WO_3, but higher than that on Co_3O_4. Furthermore, the HER process on the catalyst is also investigated (Fig. S9, ESI†). The results demonstrate that Co_3O_4 has notable activity for the HER, while the HER process on WO_3 and $CoWO_4$ is relatively slow (Fig. 1g). The above DFT calculations indicate that the $CoWO_4$ material exhibits favourable adsorption of $*NO_x$ and an efficient RDS for the conversion of $*NO_2$ to $*NO_2H$ in comparison with WO_3 and Co_3O_4. Additionally, it possesses a relatively minimized hydrolysis and HER process, which together make $CoWO_4$ have a potentially exceptional ability to reduce NO_3^- to NH_3.

3.2 Characterization analysis

Inspired by the theoretical calculations, we synthesized $CoWO_4$ nanoparticles using $Na_2WO_4 \cdot 2H_2O$ and $Co(NO_3)_2 \cdot 6H_2O$ as raw materials through a straightforward one-step precipitation method, followed by drying at 60 °C (Fig. S10, ESI†). Fig. 2a presents the X-ray diffraction (XRD) pattern of the synthesized WO_3, Co_3O_4, and $CoWO_4$. The XRD pattern indicates that the diffraction peaks of the prepared $CoWO_4$ correspond well with monoclinic $CoWO_4$ (JCPDS No. 15-0867), confirming the successful synthesis of monoclinic-phase $CoWO_4$ with a $P2/a$ space group. And the XRD patterns of the synthesized pure WO_3 and Co_3O_4 correspond well with monoclinic WO_3 (JCPDS No. 71-2141) and cubic Co_3O_4 (JCPDS No. 73-1701), respectively. The morphologies of the above synthesized catalysts were characterized by scanning electron microscopy (SEM), transmission electron microscopy (TEM), and high-resolution TEM (HR-TEM). $CoWO_4$ exhibits a particle morphology (Fig. 2b and c), which are in an aggregated state of irregular nanoparticles with a size of about 20–30 nm. And $CoWO_4$ has a more uniform and smaller nanoparticle morphology. Fig. 2d and Fig. S11 (ESI†) show the TEM images of $CoWO_4$, revealing that the nanoparticles are approximately 20 nm in size and exhibit an irregular shape. The HR-TEM image of $CoWO_4$ in Fig. 2e shows a crystalline region with an interplanar spacing of 0.46 nm, corresponding to the (001) plane of monoclinic $CoWO_4$. Additionally, Fig. 2f presents the high-angle annular dark-field scanning transmission electron microscopy (HAADF-STEM) images of $CoWO_4$ along with the corresponding energy-dispersive X-ray spectroscopy (EDS) elemental mapping images, illustrating the uniform distribution of W, Co, and O elements throughout the $CoWO_4$ nanoparticles. Fig. 2g illustrates the microscopic atomic structure model of $CoWO_4$, wherein alternating Co and W are discernible. To clarify the physical nature of the prepared $CoWO_4$ catalyst, we conducted the IR and Raman characterization of the catalysts. According to the IR and Raman profiles, the as-prepared $CoWO_4$ is monophasic (Fig. S12, ESI†). The SEM images of WO_3 in Fig. 2h and Fig. S13 (ESI†) show that WO_3 displays a significantly larger irregular nanoparticle morphology, with sizes around 200–300 nm. TEM images of WO_3 (Fig. 2i and Fig. S14, ESI†) reveal that the nanoparticles are larger, with sizes around 200–300 nm, consistent with the SEM results. The HR-TEM image in Fig. S14 (ESI†) demonstrates that the entire WO_3 lattice exhibits a highly ordered rectangular array, characterized by alternating atomic arrangements. The further magnified HR-TEM image shows
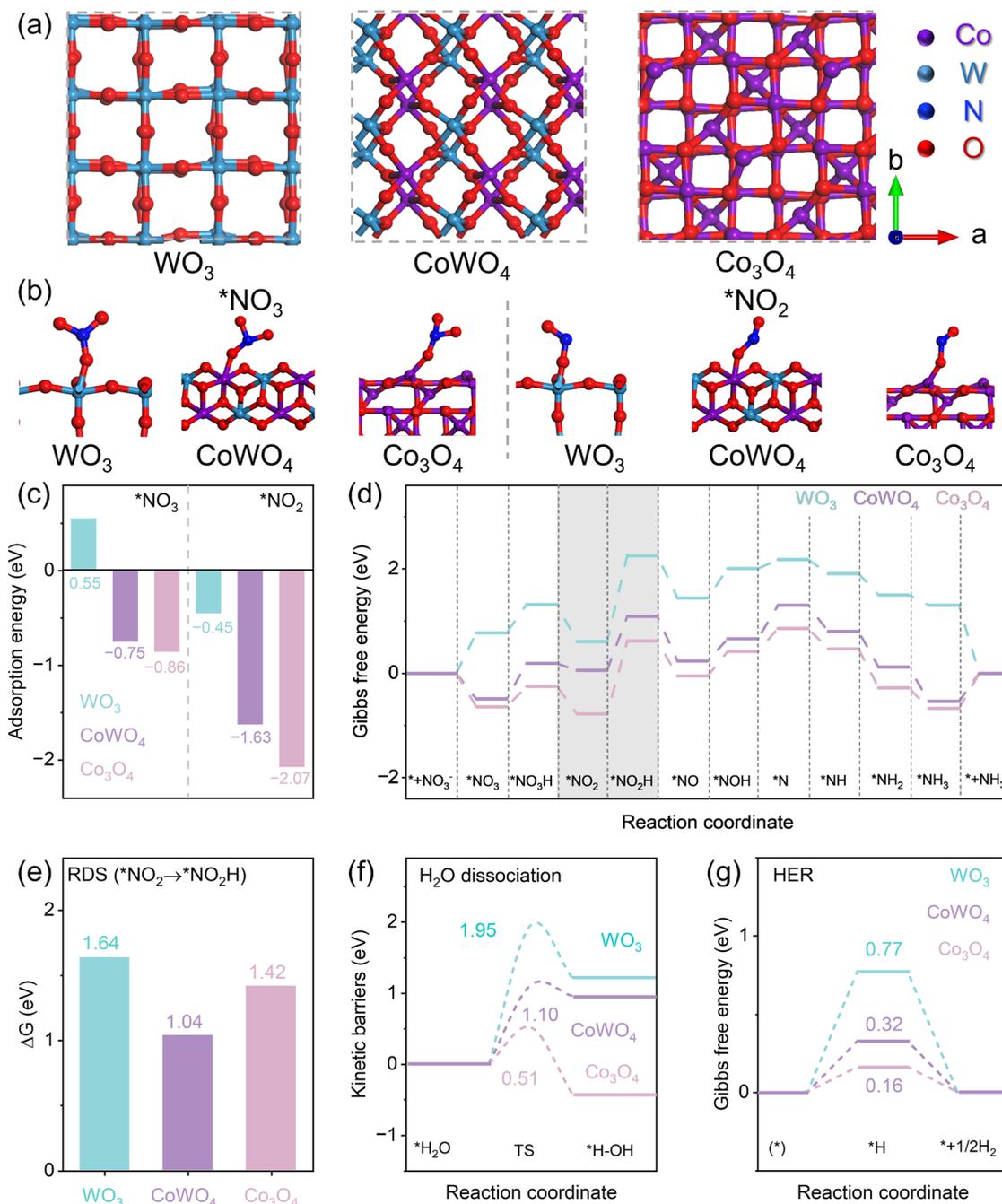
Fig. 1 (a) The atomic models of the (001) surface for WO_3, $CoWO_4$, and Co_3O_4. (b) The adsorption configurations of $*NO_3$ and $*NO_2$ intermediates on WO_3, $CoWO_4$, and Co_3O_4 surfaces. (c) The adsorption energies of $*NO_3$ and $*NO_2$ intermediates. (d) Reaction Gibbs free energies for different reaction intermediates and (e) the reaction Gibbs free energy changes (ΔG) of the RDS on the W site of WO_3, the Co site of $CoWO_4$, and the Co site of Co_3O_4. (f) Energy barrier of the H_2O dissociation process and (g) the reaction Gibbs free energy of the HER on the W site of WO_3, the W site of $CoWO_4$, and the Co site of Co_3O_4.

that the atomic spacing in the transverse and longitudinal directions is 0.38 nm and 0.37 nm, respectively, corresponding to the (002) and (020) planes of monoclinic WO_3. In contrast, Fig. 2j and Fig. S13 (ESI†) show that Co_3O_4 appears as agglomerated nanoparticles with sizes ranging from about 30 to 60 nm. The TEM images of Co_3O_4 display a relatively uniform nanoparticle morphology with an average size of approximately 40 nm (Fig. 2k and Fig. S14, ESI†). Fig. S14 (ESI†) reveals that

Co_3O_4 has good crystallinity, and the further magnified HR-TEM image shows an interplanar spacing of 0.24 nm, corresponding to the (311) plane of cubic Co_3O_4. The aforementioned study validates the successful synthesis of $CoWO_4$, WO_3, and Co_3O_4 nanoparticles.

In order to further understand the composition of the catalyst, X-ray photoelectron spectroscopy (XPS) and X-ray absorption fine structure spectroscopy (XAFS) were used to
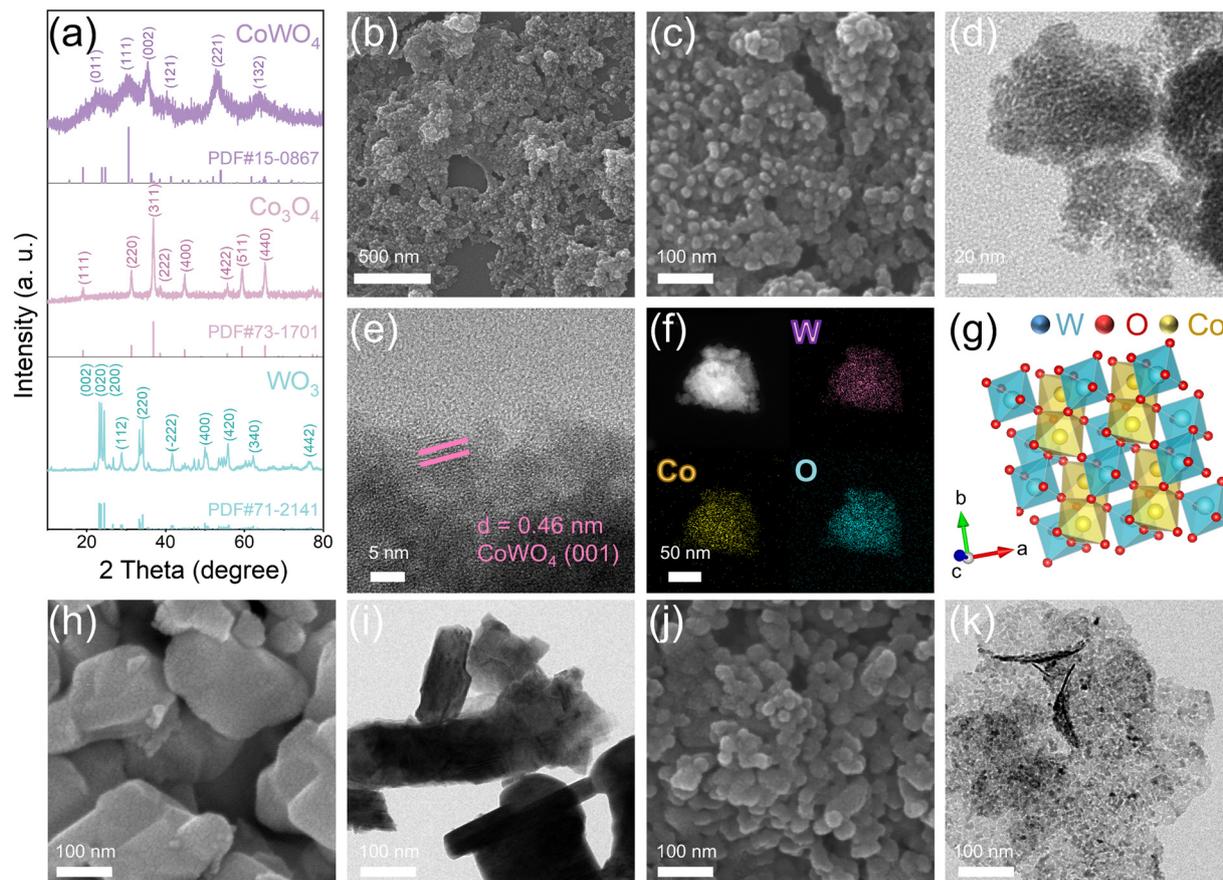
Fig. 2 (a) XRD patterns of CoWO$_4$, Co$_3$O$_4$, and WO$_3$; (b) and (c) SEM images of CoWO$_4$; (d) TEM image of CoWO$_4$; (e) HR-TEM image of CoWO$_4$; (f) HAADF-STEM image of CoWO$_4$ and the corresponding EDS elemental maps of W, Co, and O; (g) microscopic atomic structure modeling of CoWO$_4$; (h) and (i) SEM and TEM images of WO$_3$; (j) and (k) SEM and TEM images of Co$_3$O$_4$.

analyze the surface chemistry and valence state of the materials. All XPS spectra were calibrated by the C 1s peak of adventitious carbon at 284.8 eV. Fig. S15 (ESI†) shows the full XPS spectra of CoWO$_4$, WO$_3$, and Co$_3$O$_4$. The XPS full spectrum of CoWO$_4$ reveals the presence of characteristic peaks corresponding to the W, Co, O, and C elements. The carbon comes from the environments during the measurements. The absence of additional impurity peaks suggests that no additional impurity elements were introduced into the prepared samples. Fig. 3a–c show the high-resolution XPS spectra of W 4f, Co 2p and O 1s for CoWO$_4$, respectively. As shown in Fig. 3a, the XPS spectrum of W 4f shows two different split spin–orbit peaks, located at 35.2 and 37.4 eV, which correspond to a pair of typical characteristic peaks of W–O bonds (W^{6+} 4f$_{7/2}$ and W^{6+} 4f$_{5/2}$).[36,37] The XPS spectrum of Co 2p in Fig. 3b can be divided into spin–orbit peaks and satellite peaks, and the spin–orbit peaks can be divided into Co 2p$_{3/2}$ and Co 2p$_{1/2}$ regions; among them, the pair of peaks at 782.5 and 798.2 eV correspond to Co^{2+}, while the pair of peaks at 780.6 and 796.8 eV correspond to Co^{3+}, which is consistent with the reports in the literature.[38] Additionally, the two peaks at 787.1 and 803.3 eV are the satellite peaks of Co 2p.[39] In the high-resolution XPS spectrum of O 1s, as shown in Fig. 3c, the O 1s spectrum can be divided into three sub-peaks at 530.3, 531.4,

and 532.9 eV, corresponding to lattice oxygen (OL, M–O bond), defect oxygen (OD) and adsorbed oxygen (OA), respectively.[39,40] The corresponding Fourier transform magnitudes in the R space of the W L$_3$-edge demonstrates the presence of W–O bonds in WO$_3$ and CoWO$_4$ (Fig. 3d).[41] In addition, the high-resolution XPS spectra of WO$_3$ and Co$_3$O$_4$ are also characterized, which are consistent with the typical WO$_3$ and Co$_3$O$_4$ materials (Fig. S16, ESI†).[42–45] The above results prove the successful synthesis of CoWO$_4$, WO$_3$, and Co$_3$O$_4$.

3.3 Catalytic performance analysis

Subsequently, the electrochemical NO$_3$RR performance of the synthesized catalysts was investigated in an alkaline electrolyte (1 M NaOH + 0.1 M NaNO$_3$) using a typical H-type electrolytic cell. The linear sweep voltammetry (LSV) curves of the catalysts were recorded under controlled conditions. As shown in Fig. 4a, the addition of NO$_3^-$ to the electrolyte led to a significant increase in current density in all three catalysts, indicating that NO$_3^-$ actively participated in the reduction reaction, and the NO$_3$RR occurred in the solution system. CoWO$_4$ exhibits the highest current density compared to WO$_3$ and Co$_3$O$_4$. Additionally, CoWO$_4$ shows a significant increase in current density compared to the electrolyte without NO$_3^-$ (Fig. S17, ESI†), indicating its superior catalytic
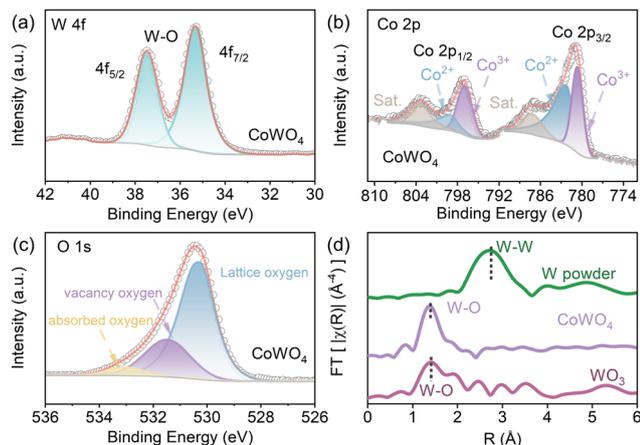
Fig. 3 High resolution XPS spectra of (a) W 4f, (b) Co 2p, and (c) O 1s for $CoWO_4$. (d) Fourier transform magnitudes in R space of the W L_3-edge for WO_3, $CoWO_4$, and W powder.

the lowest Tafel slope (310.9 mV dec^{-1}) during the NO_3RR, which is much lower than those of WO_3 (443.1 mV dec^{-1}) and Co_3O_4 (345.1 mV dec^{-1}), suggesting that the $CoWO_4$ surface has faster NO_3RR kinetics.

Then, we investigated the selectivity of electrochemical NO_3RR at different potentials. The concentrations of NH_3 and NO_2^- in the electrolyte were detected by indoxyl blue colorimetry (Fig. S18, ESI†). The faradaic efficiencies of NH_3 at varying potentials were determined through chronoamperometry and UV-visible absorbance measurements (Fig. S19, ESI†). According to the LSV curves of the catalysts, a suitable voltage range (−0.2 to −0.7 V vs. RHE) was selected to perform chronoamperometric (CA) electrolysis tests on the catalysts to more comprehensively evaluate the NO_3RR performance of the catalysts. Fig. S19a–c (ESI†) show the CA curves of $CoWO_4$, WO_3, and Co_3O_4 at different potentials. It can be seen that the current of the electrolysis reaction improves with the increase of the applied voltage. $CoWO_4$ shows the highest reaction current at each applied voltage, indicating that it has a relatively superior NO_3RR activity to WO_3 and Co_3O_4. After the electrolysis experiment, the electrolyte in the cathode chamber
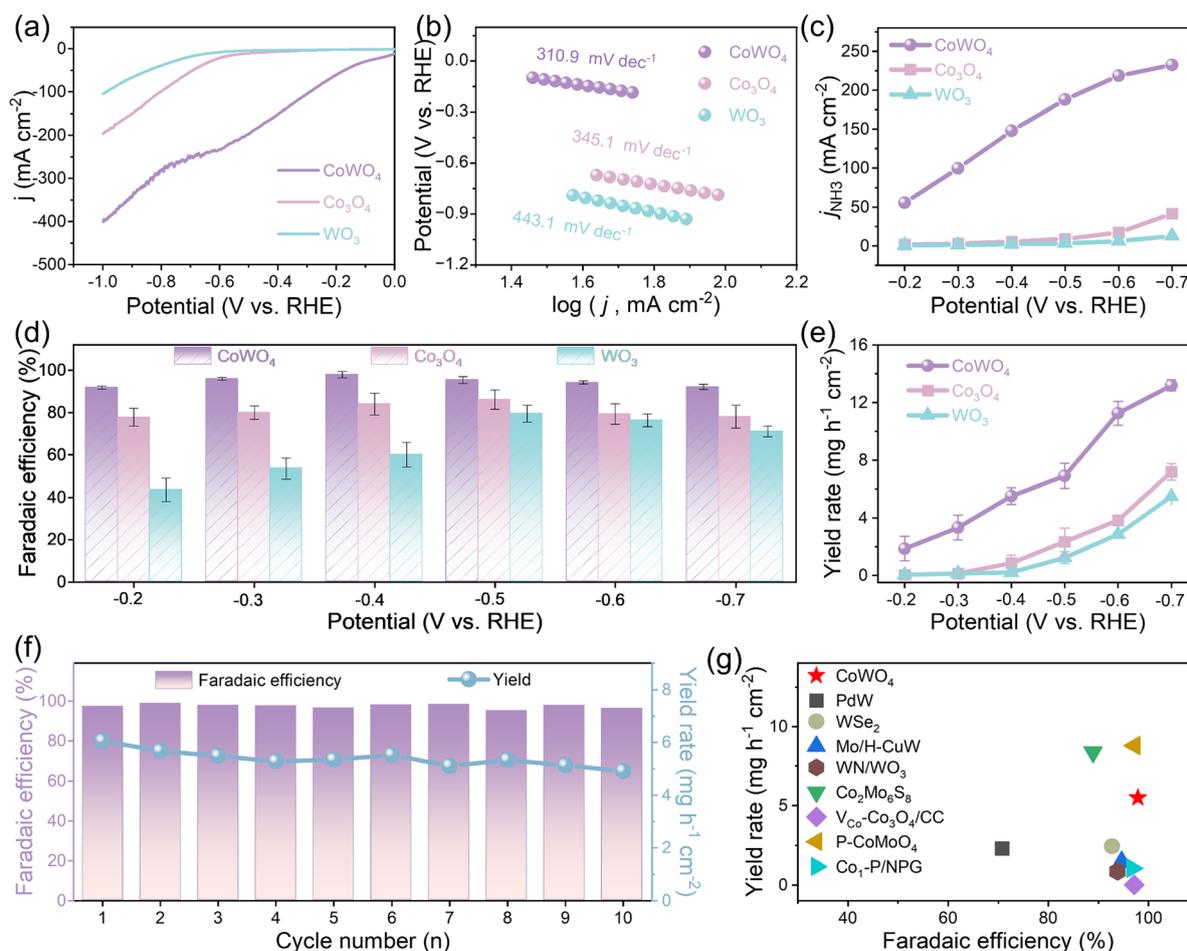
activity for the NO_3RR. And the Tafel slopes are fitted according to the LSV curves during the NO_3RR process (Fig. 4b). $CoWO_4$ has

Fig. 4 (a) LSV curves of $CoWO_4$, Co_3O_4, and WO_3 during the NO_3RR. (b) The Tafel slope derived from LSV during the NO_3RR. (c) Partial current density of NH_3 production under different potentials. (d) Faraday efficiencies of NH_3 production under different potentials. (e) Yield rate of NH_3 at different potentials. (f) FE and NH_3 yields during the cycling stability test. (g) The comparison of $CoWO_4$ with other reported catalysts.

of the electrolytic cell was collected and diluted to an appropriate concentration to determine the NH_3 content by the indophenol blue method. Fig. S19d–f (ESI†) shows the UV-visible absorption spectra of $CoWO_4$, WO_3 and Co_3O_4, respectively. The FE_{NH_3} can be calculated using the reaction current and the corresponding absorbance. The partial current density, FEs and yield rates of NH_3 under different potentials are also shown in Fig. 4c–e. It shows that the partial current density (j_{NH_3}) of $CoWO_4$ for NH_3 generation is significantly better than that of WO_3 and Co_3O_4. In addition, Fig. 4d illustrates the FE of the catalyst for NH_3 generation at various potentials. It can be seen that, with the increase of the applied potential, the FE firstly increases and then decreases, and the FE of all catalysts shows a volcano diagram trend. $CoWO_4$ shows superior selectivity and FE_{NH_3} at all potentials compared to WO_3 and Co_3O_4. The FE at all test potentials exceeds 91.7% for $CoWO_4$, which is much higher than those of WO_3 and Co_3O_4. Among them, at a potential of -0.4 V vs. RHE, the maximum FE of NH_3 generation on $CoWO_4$ can reach $97.8 \pm 1.5\%$, which is much higher than those on WO_3 ($60.1 \pm 5.8\%$) and Co_3O_4 ($83.9 \pm 5.1\%$). Based on the high selectivity and current density for NH_3 generation, $CoWO_4$ can also show a significantly higher NH_3 yield, where the yield is 5.5 ± 0.6 mg h^{-1} cm^{-2} at -0.4 V. The maximum NH_3 yield reaches 13.2 mg h^{-1} cm^{-2} at -0.7 V and the FE is 92.1% at this time, which is much higher than those of WO_3 (5.4 mg h^{-1} cm^{-2}) and Co_3O_4 (7.1 mg h^{-1} cm^{-2}). The above results suggest that $CoWO_4$ has obviously enhanced NO_3RR performance than WO_3 and Co_3O_4. To double check the production of NH_3 from $CoWO4$, Nessler's test was employed to determine the production rate of NH_3. The comparable results obtained using Nessler's reagent are shown in Fig. S20 (ESI†), confirming the great reliability of the detection results of the indophenol blue method.

The NO_3RR performances of $CoWO_4$ in low-concentration NO_3^- (100, 50, 20, and 10 mM) electrolytes were also studied. Fig. S21a (ESI†) shows the LSV curves obtained in electrolytes with different NO_3^- concentrations. As the NO_3^- concentration in the electrolyte decreases, the current response of the LSV obtained also gradually decreases, showing that the NO_3RR activity decreases accordingly. Subsequently, their NO_3RR selectivity and efficiency were studied at a voltage of -0.4 V. Fig. S21b and c (ESI†) show the corresponding chronoamperometric curves and UV curves of the solution after the reaction. The i–t curve during the reaction also shows a gradually decreasing trend with decreasing NO_3^- concentration. As shown in Fig. S21d (ESI†), $CoWO_4$ can exhibit FE_{NH_3} values of 97.9%, 94.8% and 91.8% under the electrolysis conditions of 100 mM, 50 mM and 20 mM NO_3^- concentrations, respectively. Even in the electrolyte with an extremely low NO_3^- concentration (10 mM), its FE of the NO_3RR to synthesize NH_3 is 83.4%. So, $CoWO_4$ has relatively excellent NO_3RR activity under low NO_3^- concentration electrolyte conditions. The as-prepared $CoWO_4$ materials have potential application prospects in electrocatalytic synthesis of NH_3 from wastewater.

In order to exclude the interference of other nitrogen sources that may exist in the experiment and ensure that the NH_3 produced in the experiment comes from NO_3^- in the electrolyte rather than other pollutants, a blank control experiment without NO_3^- electrolyte and without applied voltage was carried out. Fig. S22 (ESI†) shows the UV curves obtained by detecting the electrolyte under a series of different experimental conditions. Obviously, under the conditions of electrolyte without NO_3^- and electrolyte with NO_3^- without applied voltage, obvious adsorption peaks are difficult to detect in the UV curve, indicating that there is no NH_3 produced in the electrolyte. The results show that negligible amounts of NH_3 are detected in the absence of NO_3^- or without applying a voltage. However, when NO_3^- is present and a voltage is applied, a significant NH_3 yield and FE are achieved. The above results indicate that there is no contamination from any other nitrogen source during the experiment, ensuring that the NH_3 in the solution is produced from electrolytic reduction of NO_3^- in the electrolyte.

To assess the stability of the $CoWO_4$ catalyst, both cyclic electrolysis and long-term continuous electrolysis tests were carried out at a potential of -0.4 V. During the cyclic electrolysis test, the electrolyte was collected every 30 minutes for colorimetric analysis. After each cycle, the electrolytic cell was cleaned, and the electrolyte was replaced before the next cycle. The chronoamperometric curves for each cycle and the corresponding UV spectra of the electrolyte are shown in Fig. S23 (ESI†). A slight decrease in current density is observed after the first cycle, but the electrolysis current remained stable in subsequent cycles. No significant decrease is detected during the cyclic test, and the corresponding UV spectra show minimal variation. As shown in Fig. 4f, after 10 cycles, the FE and NH_3 yield of $CoWO_4$ remain stable, with the FE exceeding 96% and the NH_3 yield maintained at approximately 5.5 mg h^{-1} cm^{-2}, indicating excellent stability. Additionally, a 21-hour continuous electrolysis test was performed (Fig. S24, ESI†), without replacing the electrolyte or electrodes. The electrolyte was periodically collected for colorimetric analysis, and its UV spectra were recorded (Fig. S25, ESI†). The i–t curve in Fig. S23 (ESI†) shows stable current throughout the electrolysis, with no significant fluctuations in current density. The corresponding FE of NH_3 remains consistent throughout the test. After 21 hours, the FE is still above 88.9%. The slight decline in FE may be due to the gradual depletion of NO_3^- in the electrolyte over time. These results demonstrate the excellent electrocatalytic stability of $CoWO_4$ for the NO_3RR. Furthermore, ITO conductive glass was employed as the substrate for catalyst loading to test the XRD patterns of the catalyst before and after the electrochemical reaction (Fig. S26, ESI†). The results reveal that there is no shift in peak positions or the appearance of new peaks after the reaction, except for a reduction in the intensity of the $CoWO_4$ diffraction signal, which is likely due to catalyst detachment from the ITO substrate during the electrochemical test. The structural characterizations and the corresponding EDS elemental maps of $CoWO_4$ after reduction are shown in Fig. S27 and S28 (ESI†). The above results suggest that $CoWO_4$ exhibits excellent durability and stability for the NO_3RR to produce NH_3. Furthermore, the electrocatalytic performance of $CoWO_4$ is benchmarked against other

previously reported catalysts (Fig. 4g and Table S1, ESI†), revealing that $CoWO_4$ nanoparticles exhibit a relatively superior FE and excellent NH_3 yield, outperforming most reported Co- and W-based catalysts.[19,29,46–51]

In addition, the FEs of the byproducts (such as NO_2^-, N_2 and H_2) that may appear during the NO_3RR are also calculated. It can be seen that NH_3 and NO_2^- are the main nitrogen-containing products. Fig. S29a–c (ESI†) show the corresponding UV curves for the detected NO_2^-. According to the gas chromatograph detection results in Fig. S28d–f (ESI†), there is no N_2 detected during the reaction, and only a small amount of H_2 is detected. Fig. 5a–c show the main products of the NO_3RR of $CoWO_4$, Co_3O_4 and WO_3, respectively. As the applied voltage increases, NO_2^- is gradually converted and consumed, and the HER becomes increasingly intense. It is clearly seen that $CoWO_4$ generates fewer by-products of NO_2^- than WO_3 and Co_3O_4, which is attributed to its more favorable hydrogenation ability as predicted by DFT calculations. Meanwhile, the HER process in $CoWO_4$ is obviously decreased in comparison with WO_3 and Co_3O_4, which is well consistent with the DFT calculation results. Therefore, in comparison to WO_3 and Co_3O_4, $CoWO_4$ demonstrates a decreased HER process and a high NO_x hydrogenation ability, which together contribute to its superior capability to reduce NO_3^- to NH_3.

To deeply evaluate the intrinsic activity of these catalysts, kinetic electrochemical impedance spectroscopy (EIS) and electrochemically active surface area (ECSA) tests were conducted. Fig. 5d shows the fitted EIS of $CoWO_4$, Co_3O_4, and WO_3. The inset in the figure shows the fitting model, which includes the charge transfer resistance (R_{ct}), solution resistance (R_s) and a constant phase element (CPE). From the further enlarged EIS

graph, it can be seen that the R_s values of the three catalysts are very close. $CoWO_4$ has a significantly smaller charge transfer impedance (7.91 Ω). So, compared with WO_3 (303.80 Ω) and Co_3O_4 (194.00 Ω), $CoWO_4$ has a higher mass transfer rate during the NO_3RR and is more conducive to the reaction. The resistance values of the EIS fitted by the three catalysts are shown in Fig. S30 (ESI†) and the inserted table. Moreover, the non-polarized cyclic voltammetry (CV) curves of these catalysts were recorded at different scan rates in the potential range of 0.75–0.85 V vs. RHE, and the ECSA was evaluated by the double layer capacitance (C_{dl}) method (Fig. 5e and Fig. S31, ESI†). Fig. 5e shows the C_{dl} value calculated from the current density difference Δj at the midpoint of the measurement point interval in the CV curve and the scan rate fitting. The C_{dl} values of WO_3, Co_3O_4 and $CoWO_4$ are 0.099, 0.161 and 0.166 mF cm^{-1}, respectively. Obviously, $CoWO_4$ has the highest C_{dl} value, which indicates that it has the largest active surface area and more abundant active sites. Furthermore, to assess the intrinsic activities of these catalysts, we normalized the LSV curves by ECSA (Fig. 5f). In comparison, $CoWO_4$ continues to demonstrate the highest activity for the NO_3RR, suggesting that its enhanced catalytic performance is primarily due to the intrinsic activity of $CoWO_4$ itself.

3.4 Catalytic mechanism analysis

To verify the catalytic process, *in situ* FT-IR spectroscopy was applied to identify the reaction intermediates generated during the electrocatalytic reaction and their adsorption changes. Fig. 6a–c show the *in situ* infrared spectra of $CoWO_4$, WO_3, and Co_3O_4 for the NO_3RR at different applied potentials, respectively. The initial peak observed at 1210 cm^{-1} is indicative of the formation of $*NO_2$ (O–N–O) intermediates.[52–54]
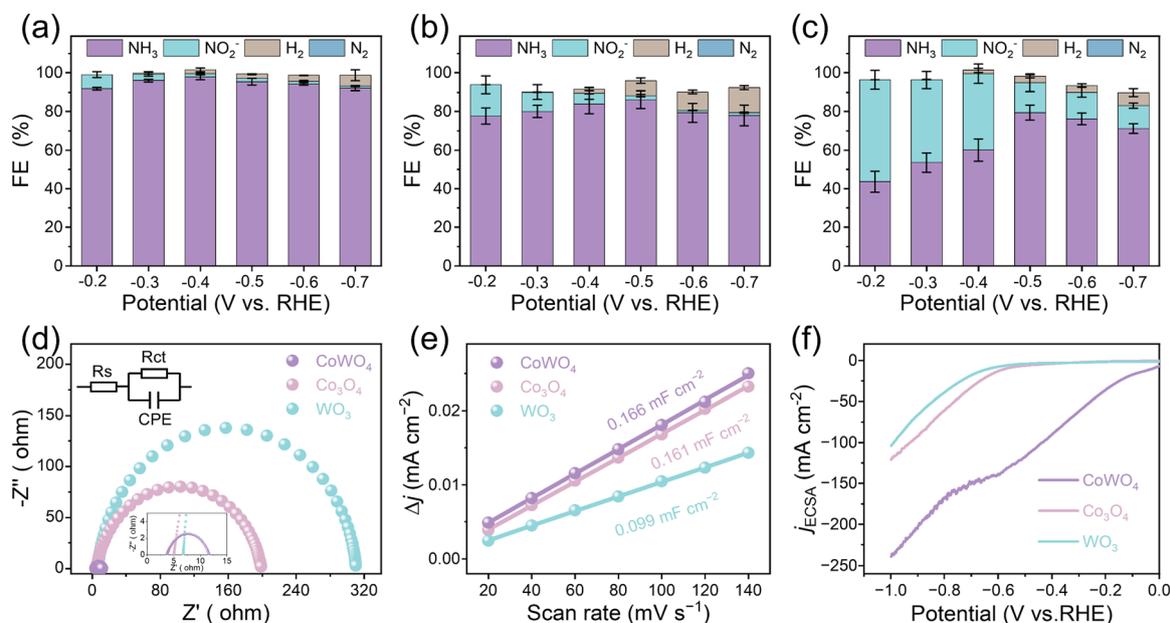

Fig. 5 (a)–(c) FEs of different products (NH_3, NO_2^-, H_2, and N_2) during NO_3RR electrolysis at various potentials for (a) $CoWO_4$, (b) Co_3O_4, and (c) WO_3. (d) The electrochemical impedance spectra of $CoWO_4$, Co_3O_4, and WO_3 (the inset shows the fitted equivalent circuit model). (e) The electrochemical active surface areas. (f) LSV curves normalized by ECSA of $CoWO_4$, Co_3O_4, and WO_3.

In comparison, the vibration peak of WO₃ at 1210 cm⁻¹ exhibits a downward shift, while the vibration peaks of CoWO₄ and Co₃O₄ display an upward shift. This suggests that *NO₂ can be accumulated on the surface of CoWO₄ and Co₃O₄, while it displays a tendency of desorption onto the surface of WO₃. This result indicates that WO₃ exhibits poor adsorption of NO₂⁻ and leads to more by-products of NO₂⁻, while NO₂⁻ is strongly adsorbed and exhibits enhanced NO₃RR activity on the surfaces of CoWO₄ and Co₃O₄. The lower peak at 1460 cm⁻¹ and the upper peak at 1585 cm⁻¹ can be ascribed to the stretching vibration of N–H in the *NH₃ intermediate, which suggests that *NH₃ is desorbed and produced NH₃ and *NH species.[55] Compared to WO₃ and Co₃O₄, these N–H vibration peaks of CoWO₄ are notably stronger, indicating the presence of significant NO₃RR processes on their surfaces. It can be clearly seen that CoWO₄ is able to enhance the hydrogenation of NO$_x$ intermediates, which is consistent with DFT calculations. Furthermore, the downward absorption band observed near 1650 cm⁻¹ is attributed to the H–O–H bending vibration of H₂O, which reflects the dissociation of H₂O on the catalyst surface.[56] The H–O–H peak is nearly absent in WO₃, indicating its limited hydrolysis performance, which hinders hydrogenation leading to formation of the byproduct NO₂⁻. In comparison, the H–O–H peak in CoWO₄ exhibits a low intensity compared to Co₃O₄, demonstrating minimized hydrolytic performance, and the HER is suppressed to some extent, which contributes to its high selectivity to NH₃. Consequently, a reaction mechanism for the NO₃RR over CoWO₄ catalysts was proposed (Fig. 6d). CoWO₄ not only enhances the adsorption and hydrogenation of *NO$_x$ intermediates but also minimizes the HER, thus facilitating a highly efficient and selective NO₃RR to produce NH₃.

4. Conclusions

In conclusion, CoWO₄ nanoparticles with Co–W dual sites have been developed to enhance the hydrogenation of *NO$_x$ intermediates and decrease the competitive HER to significantly enhance the NO₃RR for NH₃ production. Theoretical DFT calculations suggest that the Co sites in CoWO₄ facilitate the adsorption of NO$_x$ intermediates, while the W sites decrease the HER. These two sites work synergistically to promote NH₃ formation. As predicted by DFT calculations, we synthesize pure phase CoWO₄ nanoparticles by a facile ion precipitation method. The electrochemical tests demonstrate that CoWO₄ exhibits enhanced NO₃RR performance across a broader potential range (approximately −0.2 to −0.7 V $vs.$ RHE), with a faradaic efficiency
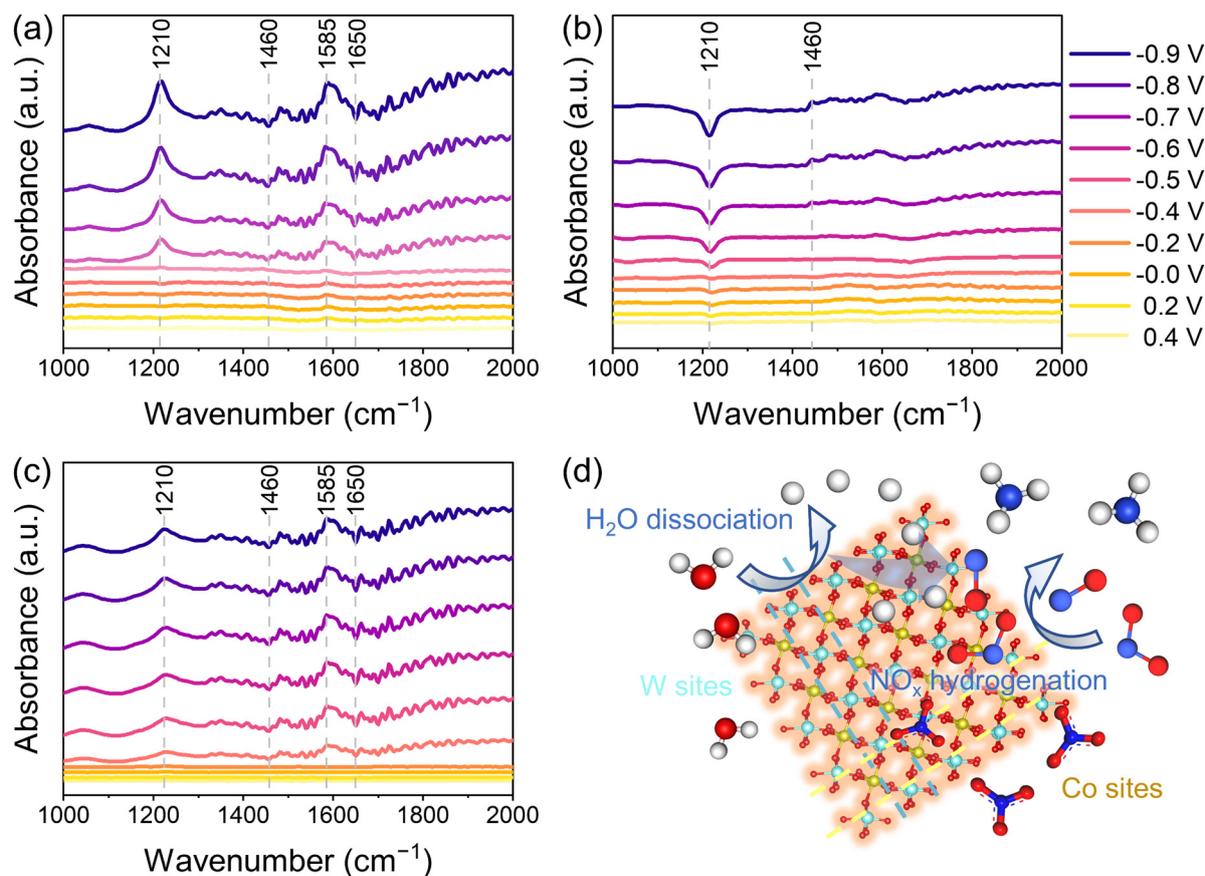

Fig. 6 *In situ* FT-IR spectra of (a) CoWO₄, (b) WO₃, and (c) Co₃O₄ at different applied potentials. (d) Proposed catalytic reaction mechanism for NH₃ formation on CoWO₄.

exceeding 91.7% at all test potentials, which is much higher than those of WO_3 and Co_3O_4 materials. Especially, the maximum FE of NH_3 generation on $CoWO_4$ is $97.8 \pm 1.5\%$ at a potential of -0.4 V, which is significantly higher than that of WO_3 ($60.1 \pm 5.8\%$) and Co_3O_4 ($83.9 \pm 5.1\%$). At a potential of -0.7 V, the maximum yield of NH_3 reaches 13.2 mg h^{-1} cm^{-2}. *In situ* FT-IR spectroscopy provides further evidence for the enhanced adsorption and hydrogenation behaviors of $*NO_x$ on $CoWO_4$ as well as decreased HER, which aligns well with the DFT calculation results. This study introduces a novel and efficient strategy for designing effective NO_3RR electrocatalysts to synthesize NH_3.

Data availability

The authors declare that all data in this manuscript are available upon reasonable request.

Conflicts of interest

The authors declare no conflicts of interest.

Acknowledgements

References

1 Z. Wu, Y. Song, H. Guo, F. Xie, Y. Cong, M. Kuang and J. Yang, *Interdiscip. Mater.*, 2024, **3**, 245–269.

2 G. Soloveichik, *Nat. Catal.*, 2019, **2**, 377–380.

3 K. Zhang, Y. Liu, Z. Pan, Q. Xia, X. Huo, O. C. Esan, X. Zhang and L. An, *EES Catal.*, 2024, **2**, 727–752.

4 G. Qing, R. Ghazfar, S. T. Jackowski, F. Habibzadeh, M. M. Ashtiani, C.-P. Chen, M. R. Smith, III and T. W. Hamann, *Chem. Rev.*, 2020, **120**, 5437–5516.

5 J. Ba, H. Dong, M. Odziomek, F. Lai, R. Wang, Y. Han, J. Shu, M. Antonietti, T. Liu, W. Yang and Z. Tian, *Adv. Mater.*, 2024, **36**, 2400396.

6 H. Zhang, K. Fang, J. Yang, H. Chen, J. Ning, H. Wang and Y. Hu, *Coord. Chem. Rev.*, 2024, **506**, 215723.

7 Y. Li, Z. Lu, L. Zheng, X. Yan, J. Xie, Z. Yu, S. Zhang, F. Jiang and H. Chen, *Energy Environ. Sci.*, 2024, **17**, 4582–4593.

8 R. Zhang, S. Zhang, H. Cui, Y. Guo, N. Li and C. Zhi, *Next Energy*, 2024, **4**, 100125.

9 Z. Wu, Y. Song, Y. Liu, W. Luo, W. Li and J. Yang, *Chem. Catal.*, 2023, **3**, 100786.

10 L. Chen, Y. Hao, J. Chu, S. Liu, F. Bai and W. Luo, *Chin. J. Catal.*, 2024, **58**, 25–36.

11 L. Cai, A. Zhang, Y. Liang, X. Fan, X. He, C. Yang, L. Ouyang, D. Zheng, S. Sun, Y. Luo, Q. Liu, S. Alfaifi, A. Farouk, M. S. Hamdy, W. Zheng, Q. Kong and X. Sun, *Mater. Today Energy*, 2023, **38**, 101428.

12 J. Liang, Z. Li, L. Zhang, X. He, Y. Luo, D. Zheng, Y. Wang, T. Li, H. Yan, B. Ying, S. Sun, Q. Liu, M. S. Hamdy, B. Tang and X. Sun, *Chem*, 2023, **9**, 1768–1827.

13 W. Zhong, Z. Gong, P. Chen, Q. Cao, X. Liu, Y. Chen and Z. Lin, *Chem. Catal.*, 2024, **4**, 101060.

14 X. Fan, D. Zhao, Z. Deng, L. Zhang, J. Li, Z. Li, S. Sun, Y. Luo, D. Zheng, Y. Wang, B. Ying, J. Zhang, A. A. Alshehri, Y. Lin, C. Tang, X. Sun and Y. Zheng, *Small*, 2023, **19**, 2208036.

15 D. Liu, L. Qiao, S. Peng, H. Bai, C. Liu, W. F. Ip, K. H. Lo, H. Liu, K. W. Ng, S. Wang, X. Yang and H. Pan, *Adv. Funct. Mater.*, 2023, **33**, 2303480.

16 Y. Xu, K. Ren, T. Ren, M. Wang, Z. Wang, X. Li, L. Wang and H. Wang, *Appl. Catal., B*, 2022, **306**, 121094.

17 X. Fan, C. Liu, Z. Li, Z. Cai, L. Ouyang, Z. Li, X. He, Y. Luo, D. Zheng, S. Sun, Y. Wang, B. Ying, Q. Liu, A. Farouk, M. S. Hamdy, F. Gong, X. Sun and Y. Zheng, *Small*, 2023, **19**, 2303424.

18 Y. Wei, J. Huang, H. Chen, S.-J. Zheng, R.-W. Huang, X.-Y. Dong, L.-K. Li, A. Cao, J. Cai and S.-Q. Zang, *Adv. Mater.*, 2024, **36**, 2404774.

19 Z. Huang, B. Yang, Y. Zhou, W. Luo, G. Chen, M. Liu, X. Liu, R. Ma and N. Zhang, *ACS Nano*, 2023, **17**, 25091–25100.

20 W. Chen, X. Yang, Z. Chen, Z. Ou, J. Hu, Y. Xu, Y. Li, X. Ren, S. Ye, J. Qiu, J. Liu and Q. Zhang, *Adv. Funct. Mater.*, 2023, **33**, 2300512.

21 T. Zhang, M.-Y. Wu, D.-Y. Yan, J. Mao, H. Liu, W.-B. Hu, X.-W. Du, T. Ling and S.-Z. Qiao, *Nano Energy*, 2018, **43**, 103–109.

22 A. Muthurasu, V. Maruthapandian and H. Y. Kim, *Appl. Catal., B*, 2019, **248**, 202–210.

23 B. Wang, X. Chen, Y. He, Q. Liu, X. Zhang, Z. Luo, J. V. Kennedy, J. Li, D. Qian, J. Liu and G. I. N. Waterhouse, *Appl. Catal., B*, 2024, **346**, 123741.

24 Y. Zhao, C. Chang, F. Teng, Y. Zhao, G. Chen, R. Shi, G. I. N. Waterhouse, W. Huang and T. Zhang, *Adv. Energy Mater.*, 2017, **7**, 1700005.

25 K. Yang, S.-H. Han, C. Cheng, C. Guo, T. Li and Y. Yu, *J. Am. Chem. Soc.*, 2024, **146**, 12976–12983.

26 M. Zhang, Z. Ma, S. Zhou, C. Han, V. Kundi, P. V. Kumar, L. Thomsen, B. Johannessen, L. Peng, Y. Shan, C. Tsounis, Y. Yang, J. Pan and R. Amal, *ACS Catal.*, 2024, **14**, 11231–11242.

27 B. Yang, Y. Zhou, Z. Huang, B. Mei, Q. Kang, G. Chen, X. Liu, Z. Jiang, M. Liu and N. Zhang, *Nano Energy*, 2023, **117**, 108901.

28 J. Wang, C. Cai, Y. Wang, X. Yang, D. Wu, Y. Zhu, M. Li, M. Gu and M. Shao, *ACS Catal.*, 2021, **11**, 15135–15140.

29 Z. Deng, C. Ma, Z. Li, Y. Luo, L. Zhang, S. Sun, Q. Liu, J. Du, Q. Lu, B. Zheng and X. Sun, *ACS Appl. Mater. Interfaces*, 2022, **14**, 46595–46602.

30 X. Wang, S. Li, Z. Yuan, Y. Sun, Z. Tang, X. Gao, H. Zhang, J. Li, S. Wang, D. Yang, J. Xie, Z. Yang and Y.-M. Yan, *Angew. Chem., Int. Ed.*, 2023, **62**, e202303794.

31 P. Liu, B. Wang, C. Wang, L. Ma, W. Zhang, E. Hopmann, L. Liu, A. Y. Elezzabi and H. Li, *Adv. Funct. Mater.*, 2024, **34**, 2400760.

32 K. Li, Y. Yin and P. Diao, *Small*, 2024, **20**, 2402474.

33 Y. Tong, H. Guo, D. Liu, X. Yan, P. Su, J. Liang, S. Zhou, J. Liu, G. Q. Lu and S. X. Dou, *Angew. Chem., Int. Ed.*, 2020, **59**, 7356–7361.

34 J. Liu, C. Tang, Z. Ke, R. Chen, H. Wang, W. Li, C. Jiang, D. He, G. Wang and X. Xiao, *Adv. Energy Mater.*, 2022, **12**, 2103301.

35 Z. Shu, H. Chen, X. Liu, H. Jia, H. Yan and Y. Cai, *Adv. Funct. Mater.*, 2023, **33**, 2301493.

36 Y. Zhao, Y. Ding, W. Li, C. Liu, Y. Li, Z. Zhao, Y. Shan, F. Li, L. Sun and F. Li, *Nat. Commun.*, 2023, **14**, 4491.

37 V. P. Singh, G. Singh, R. Patel, U. K. Gaur and M. Sharma, *J. Environ. Chem. Eng.*, 2023, **11**, 111208.

38 C. Huang, D. Wang, W. Zhang, S. J. Yoo, X. Zhou, K. Song, Z. Chen, X. Zou, N. Yue, Z. Wang, J.-G. Kim and W. Zheng, *Cell Rep. Phys. Sci.*, 2022, **3**, 101115.

39 R. Nasser, H. Zhou, F. Li, H. Elhouichet and J.-M. Song, *J. Colloid Interface Sci.*, 2024, **654**, 805–818.

40 Z. Niu, S. Fan, X. Li and G. Chen, *Adv. Energy Mater.*, 2024, **14**, 2303515.

41 Z. Wang, C. Zhu, Z. Ni, H. Hojo and H. Einaga, *ACS Catal.*, 2022, **12**, 14976–14989.

42 D. Lu, T. Liu, J. Han, J. Zhao and H. Wang, *Chem. Eng. J.*, 2023, **477**, 146896.

43 Y. Gao, R. Wang, Y. Li, E. Han, M. Song, Z. Yang, F. Guo, Y. He and X. Yang, *Chem. Eng. J.*, 2023, **474**, 145546.

44 J. Zhang, J. Liu, X. Wang, J. Mai, W. Zhao, Z. Ding and Y. Fang, *Appl. Catal., B*, 2019, **259**, 118063.

45 R. J. Colton and J. W. Rabalais, *Inorg. Chem.*, 1976, **15**, 236–238.

46 X. Li, G. Zhang, N. Zhang, Y. Luo, P. Shen, X. Li and K. Chu, *New J. Chem.*, 2022, **46**, 14724–14730.

47 D. Chen, S. Zhang, X. Bu, R. Zhang, Q. Quan, Z. Lai, W. Wang, Y. Meng, D. Yin, S. Yip, C. Liu, C. Zhi and J. C. Ho, *Nano Energy*, 2022, **98**, 107338.

48 P. Shen, G. Wang, K. Chen, J. Kang, D. Ma and K. Chu, *J. Colloid Interface Sci.*, 2023, **629**, 563–570.

49 B. Li, F. Xia, Y. Liu, H. Tan, S. Gao, J. Kaelin, Y. Liu, K. Lu, T. J. Marks and Y. Cheng, *Nano Lett.*, 2023, **23**, 1459–1466.

50 J. Ni, J. Yan, F. Li, H. Qi, Q. Xu, C. Su, L. Sun, H. Sun, J. Ding and B. Liu, *Adv. Energy Mater.*, 2024, **14**, 2400065.

51 Y. You, H. Chen, J. Guo, Z. Feng, J. Zhan, F. Yu and L.-H. Zhang, *Appl. Catal., B*, 2025, **363**, 124837.

52 N. C. Kani, N. H. L. Nguyen, K. Markel, R. R. Bhawnani, B. Shindel, K. Sharma, S. Kim, V. P. Dravid, V. Berry, J. A. Gauthier and M. R. Singh, *Adv. Energy Mater.*, 2023, **13**, 2204236.

53 H. Sun, H. Wang and Z. Qu, *ACS Catal.*, 2023, **13**, 1077–1088.

54 J.-Y. Fang, Q.-Z. Zheng, Y.-Y. Lou, K.-M. Zhao, S.-N. Hu, G. Li, O. Akdim, X.-Y. Huang and S.-G. Sun, *Nat. Commun.*, 2022, **13**, 7899.

55 Y. Zhang, H. Zheng, K. Zhou, J. Ye, K. Chu, Z. Zhou, L. Zhang and T. Liu, *Adv. Mater.*, 2023, **35**, 2209855.

56 J. Zhou, M. Wen, R. Huang, Q. Wu, Y. Luo, Y. Tian, G. Wei and Y. Fu, *Energy Environ. Sci.*, 2023, **16**, 2611–2620.